npj | Materials Degradation

www.nature.com/npjmatdeg

ARTICLE OPEN

Small molecule additives in multilayer polymer-clay thin films for improved heat shielding of steel

Carolyn T. Long[1] and Jaime C. Grunlan[1,2,3]✉

In an effort to improve the heat shielding ability of multilayer polymer-clay films, the influence of various small molecule additives was studied. Tris(hydroxymethyl)aminomethane (THAM), pentaerythritol (PER), and ammonium pentaborate (PB) are each utilized in flame retardant applications for the benefits they provide in reducing the propagation of fire. In the present study, these additives combined with polyethylenimine (PEI) and vermiculite (VMT) clay and the resulting growth of the coatings and the thermal resistivity were measured. THAM and PB salts contribute most to the overall growth of the layer-by-layer assembled films, generating an increase in film thickness of 50% or more, while PER has a greater impact on heat shielding. A 14-bilayer (THAM + PER + PEI)/VMT coating (~25 μm thick) on steel can achieve a temperature differential of over 125 °C due to a layering effect that occurs within the architecture of the macroscopic insulation bubble and disordered char. This improved thermal resistivity across a relatively thin film generates a heat shield that can be applied in novel applications such as a single-use protective barrier for aerospace components.

npj Materials Degradation (2022)6:22 ; https://doi.org/10.1038/s41529-022-00228-2

INTRODUCTION

Thermal barrier coatings (TBC) are used to protect materials from degradation upon exposure to high temperatures. Traditional TBC are ceramic-based and used predominantly for the protection of steel gas turbine blades[1,2]. More recent research is focused on polymer and polymer nanocomposite coatings as an alternative due to the potential thermal protection they can offer in tandem with their easy processability, low cost, and stability in air[3–5]. Standalone polymers are not ideal thermal barriers due to their low thermal stability, with most degrading at relatively low temperatures (> 200 °C)[6]. With that said, the ability of polymeric systems to intumesce, expand, and form an insulating char layer, has made them a viable thermal barrier in some circumstances[7,8]. Protecting structural steel, in particular, has been a focus of this research, creating a passive coating that offers protection in extreme temperature environments and prolonging the mechanical property of the steel in the event of fire[9,10]. These intumescent coatings are expendable, meant to protect the underlying substrate during extreme catastrophic events. There are a variety of other applications that can benefit from this type of single use thermal barrier coating, particularly if the coating is durable and light weight, such as the protection of spacecraft components or automobile parts. Polymer nanocomposites have the potential to offer that protection, combining the intumescent properties of polymers with the protection that is offered by ceramics in the form of nanoplatelet fillers. A recent study demonstrated how effective layer-by-layer (LbL) deposited nanocomposite coatings are for shielding steel[11].

LbL assembly is a water-based deposition technique that has been extensively used to generate thin-film polymeric coatings on solid substrates[12]. LbL coatings are produced mainly through electrostatic interactions, although hydrogen bonding and covalent bonding can be used to achieve additional functionality[13–15]. The assembly process begins by first exposing a negatively-charged substrate to a solution containing a cationic polyelectrolyte and then subsequently exposing it to an anionic solution with predetermined rinse and dry steps between to remove excess, loosely adhered material[16]. This is considered one bilayer (BL) and the steps are repeated, building on previous layers, until a desired number of bilayers is obtained. The addition of fillers, and the subsequent creation of a polymer nanocomposite, allows for nanoscale control with this technique. Utilizing this LbL assembly, filler loading levels have been demonstrated to exceed 90%[17]. In addition to this high filler loading, the layer-by-layer technique results in high alignment of clay platelets within the coating, known as a nanobrick wall structure. This creates a passive barrier mechanism that has been shown to be a highly effective gas barrier, corrosion barrier, and heat shield[18–20].

Small molecule additives have been utilized to great effect in polymer nanocomposite coatings. These additives improve the properties for applications such as semiconductors, flame retardants, and thermal barrier coatings[21–23]. Not only do these additives become incorporated into the bulk of the composite, but they often interact with the other components, influencing both the growth of LbL-assembled films and the heat shielding mechanism[24,25]. Small molecule additives have been used to promote nucleation, generate better crystallization, improve self-assembly of polymers, induce crosslinking, and increase film thickness[26–29]. In the present study, the heat shielding of nanobrick wall films is improved through the use of small molecule additives that influence the growth of the film and the architecture and charring that result from exposure to elevated temperatures.

Additives were paired with PEI, independently and together, and grown using layer-by-layer assembly, with VMT clay. LbL growth of the PEI and VMT creates the nanobrick wall structure, shown in Fig. 1, which has proven to be highly effective both as a gas barrier and fire-resistant coating[30–32]. PEI was utilized both as the mortar holding the VMT in place and as an active ingredient in the heat shielding mechanism, acting as a blowing agent during

[1]Department of Mechanical Engineering, 3123 TAMU, College Station, TX 77840, USA. [2]Department of Materials Science and Engineering, 3123 TAMU, College Station, TX 77840, USA. [3]Department of Chemistry, 3123 TAMU, College Station, TX 77840, USA. ✉email: jgrunlan@tamu.edu

Published in partnership with CSCP and USTB

npj nature partner journals

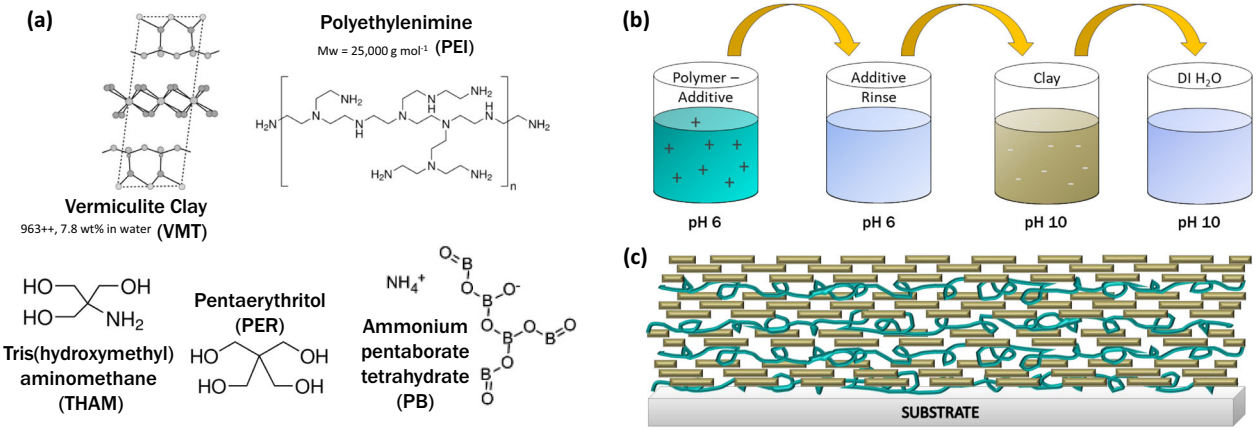

Fig. 1 Materials and methods. a Structure of polyethylenimine, vermiculite clay, tris(hydroxymethyl)aminomethane, pentaerythritol, and pentaborate. Schematics of the **b** layer-by-layer assembly process and **c** resulting multilayer nanobrick wall coating.

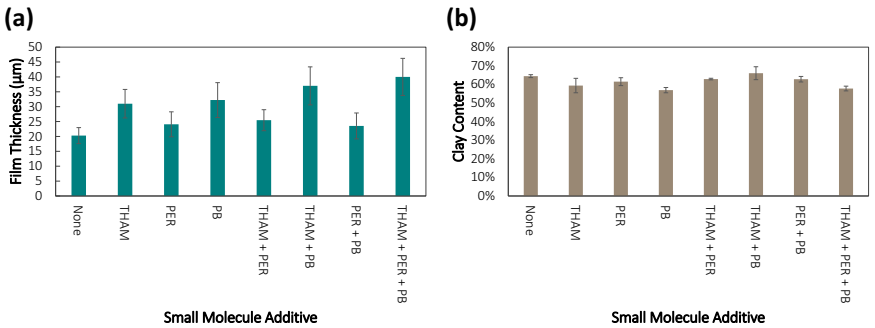

Fig. 2 Film growth. a Thickness of 14 BL PEI/VMT films with varying additive(s) and **b** clay content of films, measured using thermogravimetric analysis. Error bars are standard deviation.

pyrolysis. VMT clay was chosen as the nanoplatelet because of its high aspect ratio and thermal stability[6,33]. Small molecule additives THAM, PER, and PB were evaluated due to their unique heat-shielding characteristics. THAM has been shown to be an effective blowing agent in flame retardant and heat shielding applications[11,21,26]. Upon exposure to high temperatures, as the THAM undergoes pyrolysis, gases are released that help with the formation of a bubbled insulating layer. In flame retardant applications, PER is often utilized as an additive due to its ability to promote carbonaceous char[34,35]. Char is important because it helps to insulate the flammable substrate, cutting off one of the key contributors for fire propagation[7]. PB is a flame retardant additive used to insulate a substrate through a glassy char that has been shown to have high thermal resistivity[36,37]. When PB is exposed to temperatures in excess of 800 °C, a glassy boric oxide char is formed, which stems fire propagation and creates a more durable char[38,39].

These additives were investigated, individually and in tandem, to improve LbL film growth and the subsequent heat-shielding properties exhibited. PB is found to hinder bubble formation, reducing the overall thermal resistivity of systems containing the additive. The combination of THAM and PER outperformed the other additive groupings, providing superior thermal resistivity across a comparatively thinner film. This improved heat shielding was achieved through a combination of consistent macroscale bubble creation, a micro- and nanoscale layering porosity effect, and molecularly disordered char. These two small molecule additives work synergistically to improve the thermal resistivity of the system, offering a cost-effective heat-shielding coating that is comparable to ceramic-based thermal barrier coatings.

RESULTS AND DISCUSSION

Additive influence on film growth

Films were grown with varying combinations of THAM, PER, and PB added to the PEI solution (and cationic rinse) during layer-by-layer deposition with VMT. First, each additive was evaluated independently, then in combinations of 1:1 molar ratios, and finally all three additives were added together in a 1:1:1 ratio, using 50 mM concentration for each additive. A PEI/VMT film was also grown without any additive as a control. Each coating was grown with a 5 wt% PEI aqueous solution. The influence the additives have on film growth is shown in Fig. 2a. Both THAM and PB salts increase the growth independently by about 50%. When combined, the growth increases more than 75%, likely because more salt within the film contributes to greater charge screening and intercalation of the VMT[21,26]. PER is not a salt but still influences the growth, generating a film that is marginally thicker than the neat PEI/VMT. This is likely due to hydrogen bonding that causes more of the PEI to remain attached during the coating process. The PER acts like a crosslinker between PEI chains, which causes a greater amount of PEI to adhere in a single deposition step. The addition of the PER can also be seen to mitigate some of the thickening effects of the other additives. THAM + PER and PB + PER are thinner than their individual salt counter parts. The hydrogen-bonded crosslinking, created with the addition of the PER, constrains the PEI and therefore hinders the thickening effect of the charge screening. Conversely, films grown with all three additives do not suffer from any impediment PER causes, instead generating a thickness roughly double that of the neat PEI/VMT film. For these samples, with a greater extent of salt in the deposition solution, the thick growth influenced by the charge

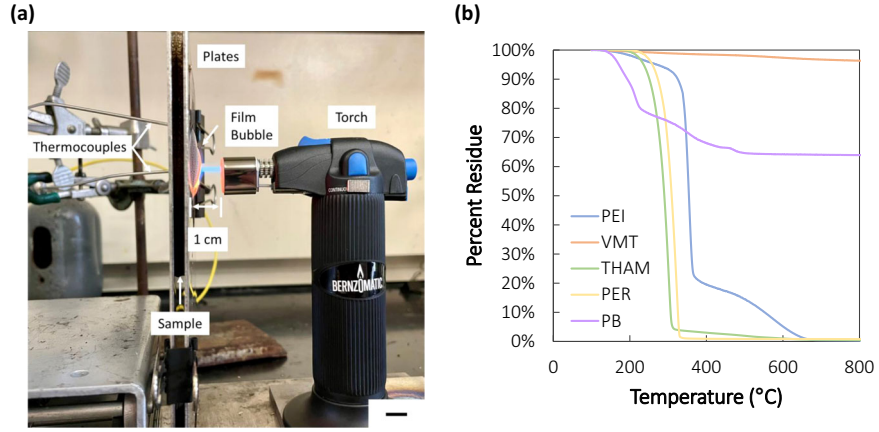

Fig. 3 Test setup and TGA of materials. a Digital image of the flame test setup, with components and sample labeled, and **b** thermogravimetric analysis of the individual materials used in making the multilayer films. Scale bar for digital image is 1 cm.

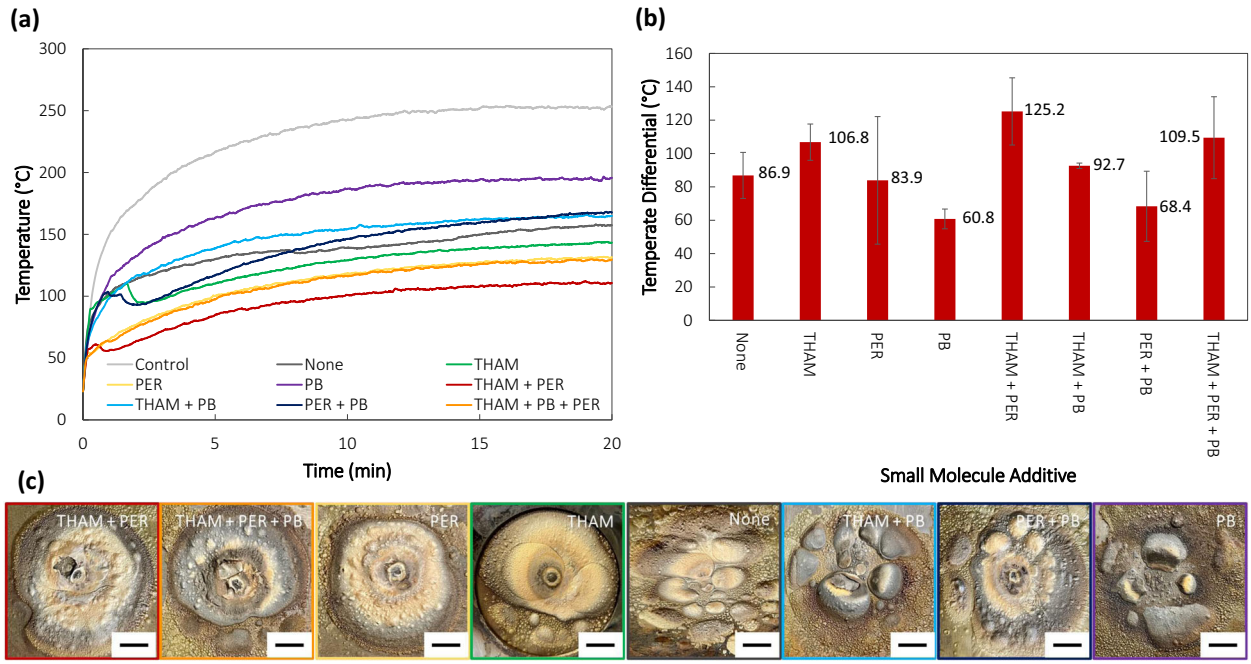

Fig. 4 Flame testing results. a Temperature curves during torch testing of 14 BL films on steel, **b** the resultant temperature differential when compared to the uncoated control substrate (ΔTfilm = Tmax,control − Tmax,film), and **c** the morphology of each of the samples following the torch testing, shown in order from best performing to worst. Error bars are standard deviation and scale bars are 1 cm.

screening works in tandem with the hydrogen-bonded cross-linking from the PER. This results in a greater amount of PEI being deposited more densely with each BL. From Fig. 2b, it appears that the additives have no apparent influence on the amount of clay deposited in each sample.

Multilayer coating heat shielding

Films with varying additives were tested by exposing the coated side of the steel to the flame from a butane torch for 20 min and compared by recording the temperature change on the back side (i.e., uncoated side) of each sample. Figure 3a shows the setup of the flame test. In tandem with film testing, the individual components were evaluated with thermogravimetric analysis (TGA) (Fig. 3b). PEI and two of the additives, THAM and PER, decompose completely before 400 °C, undergoing pyrolysis and releasing gases. When PB is exposed to high temperatures, instead of completely decomposing, it forms a boric oxide glassy residue. VMT remains stable at high temperatures, but a slight reduction in weight can be seen as the surfactants that are part of the aqueous suspension decompose. Upon exposure to flame, the PEI and additives in the sample undergo pyrolysis, degrading and releasing gases. The gases become trapped between the remaining clay-filled char layer and the steel, forcing the film to expand to form an insulating shell. Films with PB likely generate a more durable char due to the presence of the boric oxide. Ultimately, though the char may have higher strength, the boric oxide hinders the expansion of the insulating shell, which results in poorer shielding performance.

The temperature curves for each of the samples during the 20 min of flame testing can be seen in Fig. 4. As detailed in a previous study, the formation of a large bubble is paramount to achieving high thermal resistivity[11]. Generally, the films with PB perform poorly, with the film containing the individual pentaborate additive only obtaining a 60 °C differential. This is likely due to the glassy residue that PB generates, which restricts the growth of the protective bubble. The film without any additives

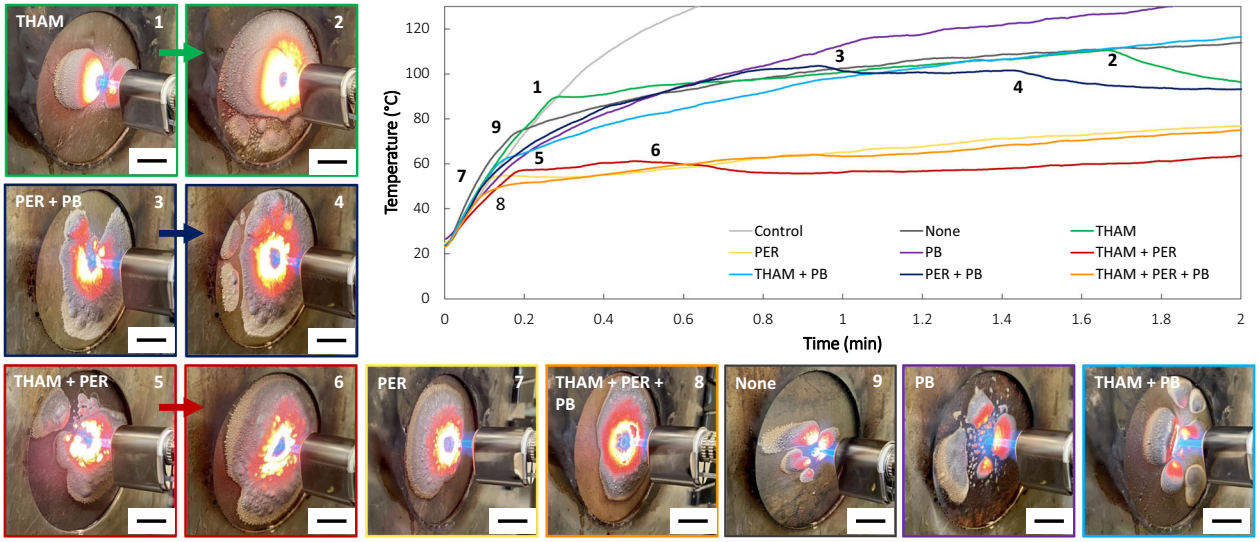

Fig. 5 Formation of Insulating Bubbles. Formation of macroscale bubbles and the backside recorded temperature of the steel for each of the film types: No additive (gray), THAM (green), PER (yellow), PB (purple), THAM + PER (red), THAM + PB (blue), PER + PB (navy), and THAM + PER + PB (orange). Numbered points on the graph correspond to the surrounding film images. Scale bars are 1 cm.

outperformed the PB and PB + PER films, likely due to the high level of polymer available for blowing. The only film with PB that has consistent bubble generation is the film with all of the additives (i.e., THAM + PER + PB). For this film, the combined effects of the THAM and PER largely overcome the limitations of the PB additive. This combined sample, in addition to films containing individual THAM and PER (and THAM + PER) generate higher thermal resistivities and exhibit consistent bubble formation. Of the additives tested, the THAM + PER films outperform all the other samples. Not only does THAM + PER generate the greatest temperature differential, but it also has a significantly larger thermal resistivity as the heat is dissipated across a thinner film. Comparing the samples with just THAM to the combined THAM + PER in this study, the THAM + PER samples garner about 20 °C greater temperature differential across a film that is 5 µm thinner. To evaluate if this result simply stems from the presence of more additive, the growth of the films and the subsequent thermal resistivity were evaluated for THAM + PER at ratios of 3:1 and 1:3 (see Supplementary Fig. 1 in Supplemental Information). No difference in film growth is observed with changing ratio, but there is a reduction in shielding performance, as one or the other of the additive mechanisms dominates. Consequently, the superior performance of THAM + PER is a result of the combined mechanisms, each acting in tandem to improve the thermal resistivity.

The eventual formation of the bubble, or not, is generally consistent, but the exact timing and scale of the bubble is driven by the entropic nature of pyrolysis. The initial few minutes of testing has the most activity and is often predictive of how the film will perform overall. Figure 5 focuses on the first two minutes of torch testing and highlights the bubble formation and resulting influence on thermal diffusivity. Definitive changes in the temperature recorded for various samples can be seen. These sharp changes in temperature occur initially when the bubble first starts to grow, particularly as the film is forced away from the steel and a pocket of gas insulates it. This gaseous insulation improves when the bubble expands, as seen in points 2, 4, and 6. In each instance, the temperature temporarily decreases as the heat must traverse a greater distance to get to the vulnerable steel. This highlights the importance of the macroscale bubble in creating an effective thermal barrier.

Influence of bubble architecture

Material architecture has long been understood to be an integral part of the thermal resistance exhibited by heat shielding coatings. Films with pores generate greater thermal resistivity, whereas coatings with a greater level of filler interconnectivity can increase thermal conductivity[40–42]. For some of the samples, particularly those with THAM and PER as the additives, the bubble created is comparable on the macroscale level, each taking a large area of the testing space. To evaluate the difference between these coatings, the structure and char formation of the bubbles are evaluated. Figure 6 shows cross-sectional images of the four best performing films after testing, along with optical microscope images. The film that was grown with only THAM creates a cohesive macroscale bubble, with one large cavity, and is the only film that can be sheared to see the internal structure. The intermolecular bond strength of films with THAM is greater than the films grown with other additives, causing the film to be more durable, even after burning. This is likely because the hydrogen bonds formed between THAM and PEI are stronger as the NH_2 groups preferentially bond.

Bubbles formed by films without THAM, or with additional additives alongside, do not exhibit the same singular cavity between film and substrate. Optical images of these bubbles show that films with PER as one of the additives exhibit layering. This layered bubbling generates even greater thermal resistivity from the additional microdomains the energy must travel through. These pockets result as gases released during pyrolysis not only separate the film from the substrate but also delaminates the clay platelet layers. In the case of the film containing both THAM and PER, the two additives work synergistically to create a larger bubble, similar in scale to the neat THAM bubble, and the layering effect that diminishes heat transfer across the system. The addition of PB to the system results in reduced performance. While the THAM and PER still work in tandem to generate a large, layered bubble, the boric oxide from the PB still hinders the growth of the bubble, lessening the overall thermal resistance of the film.

Another key feature in the architecture of the films after pyrolysis is nanodomains. SEM images of the samples where the film was directly exposed to the flame, shown in Fig. 7, reveal nano-characteristics that mimic the macroscale analysis. Three of the films (THAM + PER, PER, and THAM) exhibit nanoporosity. This nanoporosity results as the film intumesces and gases are trapped. Nanoporosity in thermal barrier coatings has been demonstrated

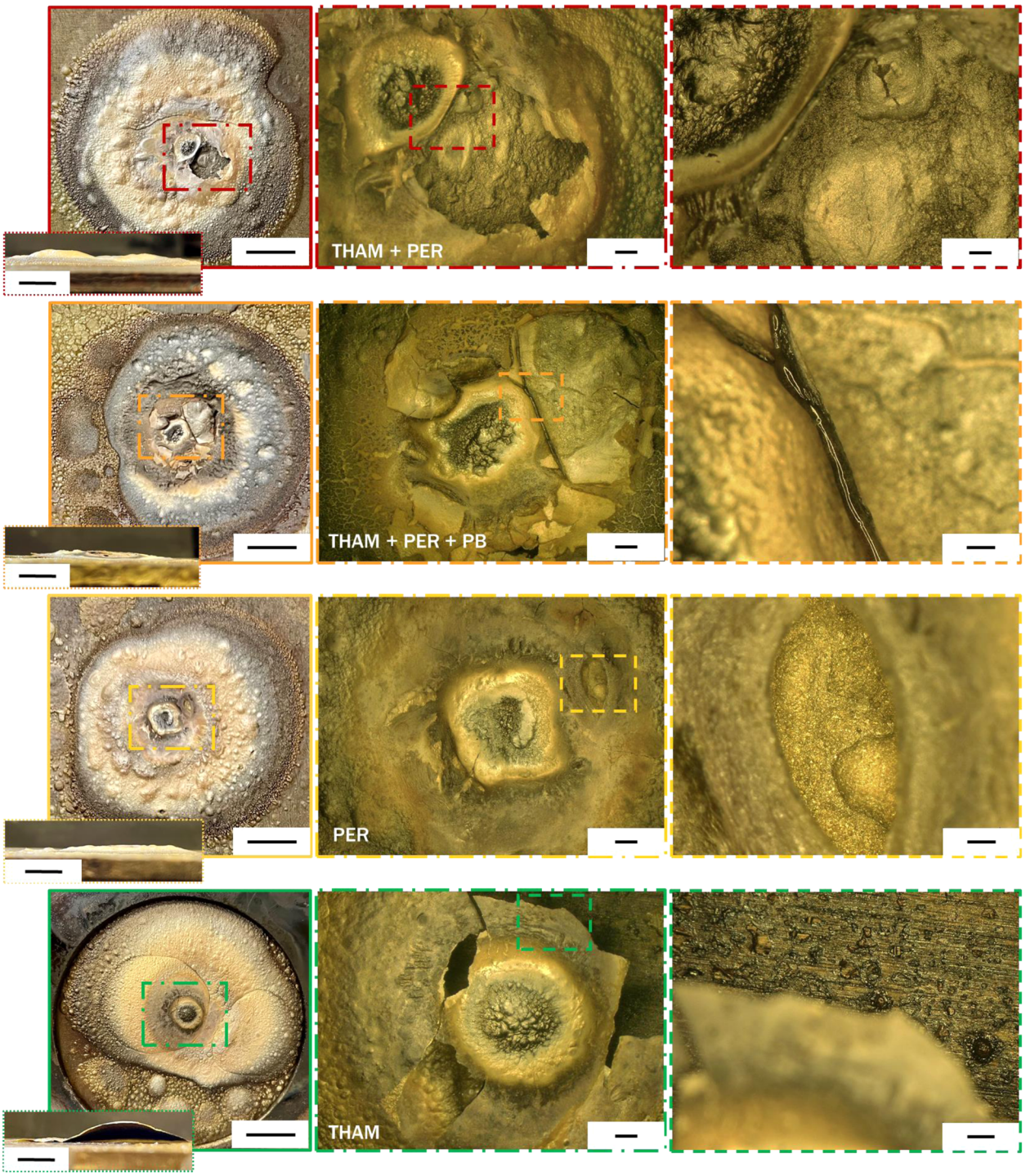

Fig. 6 Digital and optical imaging. Digital and optical images of 14 BL films with THAM + PER (red), THAM + PER + PB (orange), PER (yellow), or THAM (green) after torch testing and corresponding cross-sectional image of each. Across each row, each image is progressively zoomed in views of the bubble architecture. Scale bars for cross-sectional images and macroscale bubble images (on the left) are 1 cm. Scale bars for middle images are 1 mm. For far right images the scale bars are as follows: 300 µm for THAM + PER (red), 250 µm for THAM + PER + PB (orange), 250 µm for PER (yellow), and 500 µm for THAM (green).

to be effective at hindering thermal transport due to phonon scattering[43–45]. The film with the combined additives (THAM + PER + PB) does not display nanoporosity. While a macroscale bubble and layering result when the THAM and PER undergo pyrolysis, the PB that limits the bubble formation also likely hinders nanopore formation. In addition to the nanoporosity, the PER film shows signs of microscale layering. Like the larger pockets, these smaller pockets hinder thermal diffusion and provide additional surface for the presence of the intumesced bubbles to generate upon. The film with just THAM exhibits extensive nano- and microporosity but the cohesion in the film limits the expansion of these bubbles. The THAM + PER film manifests this same microscale porosity but to a greater extent, as the bubbles are larger and layered pockets are evident. This mimics the macroscale analysis in that THAM and PER

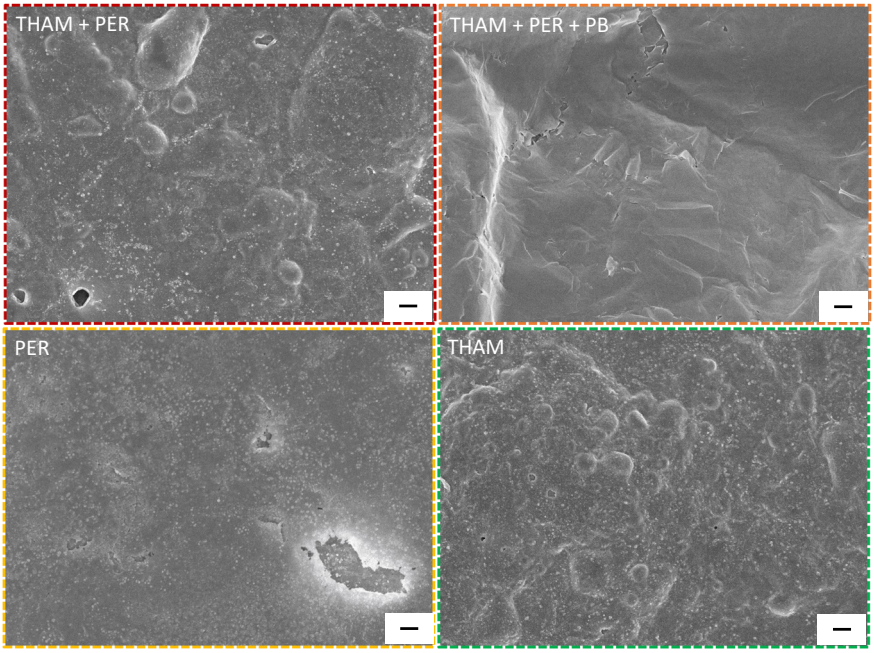

Fig. 7 SEM imaging. SEM images of 14 BL films with varying additives: THAM + PER (red), THAM + PER + PB (orange), PER (yellow), and THAM (green). Nanoporosity and microscale layering and bubbling, which contribute to the overall film thermal resistivity, can be observed. Scale bars are each 1 μm.

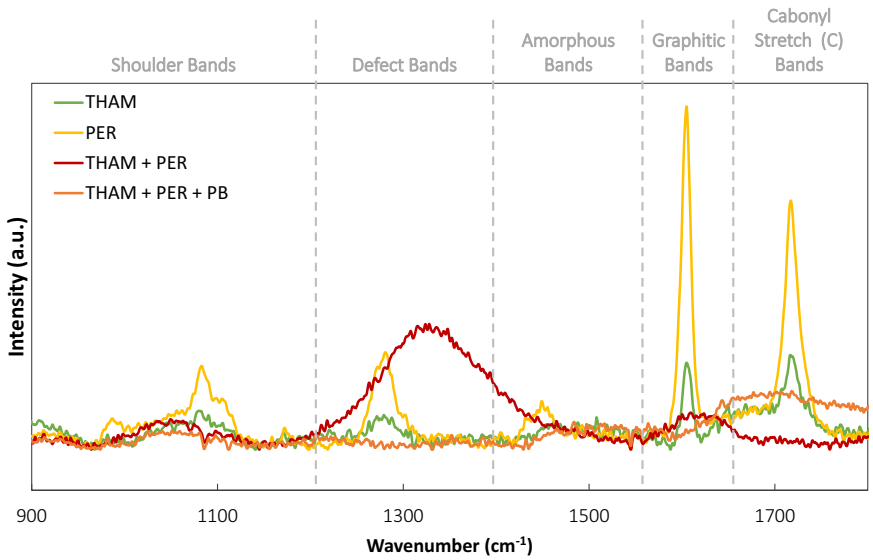

Fig. 8 Char Raman analysis. Raman spectra of 14 BL films after torch testing, showing definitive differences in the charring exhibited by the samples containing THAM (green), PER (yellow), THAM + PER (red), and THAM + PER + PB (orange).

contribute equally to the physical architecture of the intumesced coating and to the corresponding overall mechanism of heat shielding.

In addition to physical structure, the molecular architecture of the material influences the thermal resistivity of the system. Figure 8 shows the Raman analysis of the burnt films, which provides insight into the morphology and extent of char generated by each of the best performing samples. Measurements were done using the neat PEI/VMT samples as the internal reference. The bands of interest are the graphitic and defect bands, G-bands and D-bands, respectively[46]. The degree of disorder in carbonaceous materials can be described by the ratio of the intensity of the D-band peak relative to the G-band peak (I_D/I_G), where a larger ratio indicates greater disorder. The films with THAM and PER, independent of each other, have a distinct, sharp peak in the graphitic range. This high frequency band is caused by the vibrational frequency of high energy sp^2 bonded carbon. The Lorentzian style peak is indicative of well-ordered crystalline graphitic char[47]. For the PER film, for which the G-band peak is the most intense, the sp^2 carbon bonds are the most prominent in the resultant char. Additionally, the G-band peak, and others, are largely more intense, indicating a greater extent of charring is present, which likely contributes to improved heat shielding. THAM, which is not a char promoter, displays a similar spectrum of carbon bonding as the PER film, but the peaks have lower intensity, so less charring is present. Conversely, the film containing THAM and PER together exhibits a low-profile Gaussian curve in the graphitic band region, which is representative of disorder and defects in the graphene[48]. The larger intensity curve in

the defect band region, and consequently the larger I_D/I_G ratio, is a further indication of the disordered nature of this sample's char. The disordered atomic morphology results in more energy needed for thermal carriers to transport heat to neighboring sites[49,50]. This results in a loss of energy and subsequently less heat transferred. By contrast, graphitic char is thermally conductive, so even though there is more charring present it does not stem the heat as effectively. The film with the combined THAM, PER, and PB does not have any definitive peaks, likely because any carbonaceous charring that results is dominated by the boric oxide.

Small molecule additives tris(hydroxymethyl)aminomethane, pentaerythritol, and pentaborate have a direct influence on the growth and heat shielding exhibited by PEI/VMT multilayer films. Each contributes to the film thickness, though THAM and PB contribute to substantially thicker growth due to charge screening of the polymer. The insulating role of the macroscale bubble is highlighted, as samples that do not form a cohesive bubble offer less thermal resistivity. This is particularly evident in films containing PB, which forms boric oxide at high temperatures that hinders the bubble creation. The most successful heat-shielding coating contains PER and THAM together. THAM + PER films combine thermal resistance mechanisms from the two additives to create a more effective barrier, which stems a greater amount of heat transfer across a thinner film. Fourteen bilayer films, when exposed to elevated temperatures, consistently create large macroscale bubbles that exhibit a layering effect, in both the macro- and nanoscale domains, in addition to disordered char at the molecular level. Consequently, the two additives working together most effectively stems heat transfer through the combination of energy lost in the transport between various micro- and macrodomains, phonon scattering in nanodomains, and poor thermal diffusion along disordered molecular char.

METHODS

Materials and substrates

Branched polyethylenimine (PEI) ($M_w = 25{,}000\ g\ mol^{-1}$), tris(hydroxymethyl)aminomethane (THAM, crystalline), ammonium pentaborate tetrahydrate (PB, ≥ 99%), and pentaerythritol (PER, 98%) were purchased from Sigma-Aldrich (Milwaukee, WI). Microlite 963++ vermiculite clay (VMT, 7.8 wt % in water) was purchased from Specialty Vermiculite Corp (Cambridge, MA). Deionized (DI) water, with a resistivity equal to 18 MΩ, was used to prepare all solutions and rinses. Films were grown using an aqueous solution containing 5 wt % PEI, combined with 50 mM additives. Additives were added independently (THAM, PB, and PER), and in combinations (THAM + PB, THAM + PER, PER + PB, and THAM + PER + PB), mixed into the PEI solution and the cationic rinse. Additive solutions were prepared prior to adding the PEI. VMT was diluted to a 1 wt % suspension and stirred overnight prior to use. The cationic solution and corresponding rinse pH were adjusted to 6, and the anionic solution and rinse pH were adjusted to 10, using 5 M HCl and NaOH, respectively. A36 ground low-carbon steel was purchased from McMaster Carr (Aurora, OH) as 10.16 cm × 10.16 cm × 0.32 cm plates. Metal substrates were cleaned with a DI water rinse followed by a methanol rinse and then DI water rinses again to remove any large debris. This was followed by bath sonicating in DI water and then isopropanol (IPA) for 2 min each, with IPA rinses between, before being dried with filtered air. The steel was then immersed in a 1 M sodium hydroxide and 100 mM sodium nitrite solution overnight to passivate the surface for better adhesion prior to deposition.

Thin film preparation

Steel substrates were coated with PEI/VMT multilayers using layer-by-layer (LbL) assembly, which was carried out with a home-built robotic system[51]. Prior to deposition, one side of the steel was taped off to ensure an uncoated side for testing. Films were assembled by first immersing the substrate into a polycationic solution for 5 min, followed by dipping in a rinse solution containing the additive(s) for 1 min. From there, the substrate was immersed in the anionic clay solution for 5 min, and then dipped into a DI water rinse for 1 min, which completes one bilayer (BL). Subsequent bilayers use 1 min dips in each solution. The process was repeated until the desired number of bilayers were deposited. Once all the bilayers were deposited, films were dried in ambient conditions overnight and then stored in a desiccant box prior to testing. All films were prepared with 14 BL, varying the additive species amongst samples. A schematic of the deposition procedure, and resulting nanobrick wall structure, is shown in Fig. 1.

Torch testing

Steel samples were mounted between two A36 steel plates (15.24 cm × 20.32 cm), with a 5.08 cm diameter circle hole to access the sample from front and back. A K-type thermocouple (McMaster-Carr; Aurora, OH) was mounted on the back side of the steel plate in the center of the hole. Silver conductive paint (Electron Microscopy Science; Hatfield, PA) was used to improve thermal contact between the steel plate and the thermocouple. A butane torch (Bernzomatic precision torch ST2200T; Worthington Industries, Columbus, OH) was oriented perpendicularly to the coated side of the sample and a flame was applied for 20 min. The nozzle of the butane torch was placed 1 cm away from the sample and in line with the thermocouple. Coated steel samples were compared to an uncoated steel plate tested under the same conditions.

Nanocomposite film characterization

Individual additives and each type of film were analyzed with a Q50 Thermogravimetric Analyzer (TA-instruments; New Castle, DE). Films weighing approximately 7–9 mg were tested in an air atmosphere. First, the materials were held at 120 °C for 20 min to remove water, then the temperature was increased at a heating rate of $10\ °C\ min^{-1}$. The clay composition of the freestanding films was measured using the same process. The thickness of films was measured using a dial indicator (Chicago Dial Indicator Co.; De Plaines, IL). The surface morphologies of the films after burning were observed with optical microscope (Keyence VHX-600K Digital Microscope; Itasca, IL) and then additional imaging was obtained using a field-emission scanning electron microscope (SEM) (model JSM-7500, JEOL; Tokyo, Japan). Prior to imaging, samples were sputter-coated with 5 nm of platinum/palladium. Raman spectroscopy (Horiba Jobin-Yvon LabRam HR Raman confocal microscope; Kyoto, Japan) was done to analyze the type and extent of char each film generated. Films were scanned between 800 and 2000 cm^{-1} using a 633 nm laser with 300 gr mm^{-1} grating.

DATA AVAILABILITY

The data that support the finding of this study are available from the corresponding author upon request.

Received: 22 October 2021; Accepted: 8 February 2022;
Published online: 22 March 2022

REFERENCES

1. Thakare, J. G., Pandey, C., Mahapatra, M. M. & Mulik, R. S. Thermal barrier coatings—A state of the art review. *Met. Mater. Int.* **27**, 1947–1968 (2020).
2. Vaßen, R., Jarligo, M. O., Steinke, T., Mack, D. E. & Stöver, D. Overview on advanced thermal barrier coatings. *Surf. Coat. Technol.* **205**, 938–942 (2010).
3. Azadi, M., Baloo, M., Farrahi, G. H. & Mirsalim, S. M. A review of thermal barrier coating effects on diesel engine performance and components lifetime. *Int. J. Automot. Eng.* **3**, 305–317 (2013).
4. Feih, S., Mouritz, A. P., Mathys, Z. & Gibson, A. G. Fire structural modeling of polymer composites with passive thermal barrier. *J. Fire Sci.* **28**, 141–160 (2010).
5. Yew, M. C. & Sulong, N. H. Ramli Fire-resistive performance of intumescent flame-retardant coatings for steel. *Mater. Des.* **34**, 719–724 (2012).
6. Liu, L., Yu, Z.-L., Qu, J. & Huang, J. Spray-coated barrier coating on copper based on exfoliated vermiculite sheets. *Mater. Chem. Front.* **5**, 4658–4663 (2021).
7. Lazar, S. T., Kolibaba, T. J. & Grunlan, J. C. Flame-retardant surface treatments. *Nat. Rev. Mater.* **5**, 259–275 (2020).
8. Luangtriratana, P., Kandola, B. K., Duquesne, S. & Bourbigot, S. Quantification of thermal barrier efficiency of intumescent coatings on glass fibre-reinforced epoxy composites. *Coatings* **8**, 347 (2018).
9. Lucherini, A. & Maluk, C. Intumescent coatings used for the fire-safe design of steel structures: A review. *J. Constr. Steel Res.* **162**, 105712 (2019).
10. Ustinov, A., Zybina, O., Tanklevsky, L., Lebedev, V. & Andreev, A. Intumescent coatings with improved properties for high-rise construction. *E3S Web Conf.* **33**, 02039 (2018).
11. Long, C. T. et al. Efficient heat shielding of steel with multilayer nanocomposite thin film. *ACS Appl. Mater. Interfaces* **13**, 19369–19376 (2021).

12. Rawtani, D. & Agrawal, Y. K. Emerging strategies and applications of layer-by-layer self-assembly. *Nanobiomedicine* **1**, 8 (2014).
13. Bergbreiter, D. E. & Liao, K.-S. Covalent layer-by-layer assembly—an effective, forgiving way to construct functional robust ultrathin films and nanocomposites. *Soft Matter* **5**, 23–28 (2009).
14. Lyklema, J. & Deschênes, L. The first step in layer-by-layer deposition: Electrostatics and/or non-electrostatics? *Adv. Colloid Interface Sci.* **168**, 135–148 (2011).
15. Qin, S., Song, Y., Floto, M. E. & Grunlan, J. C. Combined high stretchability and gas barrier in hydrogen-bonded multilayer nanobrick wall thin films. *ACS Appl. Mater. Interfaces* **9**, 7903–7907 (2017).
16. Borges, J. & Mano, J. F. Molecular interactions driving the layer-by-layer assembly of multilayers. *Chem. Rev.* **114**, 8883–8942 (2014).
17. Priolo, M. A., Holder, K. M., Gamboa, D. & Grunlan, J. C. Influence of clay concentration on the gas barrier of clay–polymer nanobrick wall thin film assemblies. *Langmuir* **27**, 12106–12114 (2011).
18. Hagen, D. A. et al. High gas barrier imparted by similarly charged multilayers in nanobrick wall thin films. *RSC Adv.* **4**, 18354–18359 (2014).
19. Laufer, G., Kirkland, C., Cain, A. A. & Grunlan, J. C. Clay–chitosan nanobrick walls: Completely renewable gas barrier and flame-retardant nanocoatings. *ACS Appl. Mater. Interfaces* **4**, 1643–1649 (2012).
20. Qin, S. et al. Ultrathin transparent nanobrick wall anticorrosion coatings. *ACS Appl. Nano Mater.* **1**, 5516–5523 (2018).
21. Guin, T. et al. Exceptional flame resistance and gas barrier with thick multilayer nanobrick wall thin films. *Adv. Mater.* **2**, 1500214 (2015).
22. He, Z., Zhang, Z., Bi, S., Chen, J. & Li, D. Conjugated polymer controlled morphology and charge transport of small-molecule organic semiconductors. *Sci. Rep.* **10**, 4344 (2020).
23. Hutton-Prager, B., Khan, M. M., Gentry, C., Knight, C. B. & Al-Abri, A. K. A. Thermal barrier enhancement of calcium carbonate coatings with nanoparticle additives, and their effect on hydrophobicity. *Cellulose* **26**, 4865–4880 (2019).
24. Stevens, D. L., Gamage, G. A., Ren, Z. & Grunlan, J. C. Salt doping to improve thermoelectric power factor of organic nanocomposite thin films. *RSC Adv.* **10**, 11800–11807 (2020).
25. Tang, K. & Besseling, N. A. M. Formation of polyelectrolyte multilayers: Ionic strengths and growth regimes. *Soft Matter* **12**, 1032–1040 (2016).
26. Lazar, S., Eberle, B., Bellevergue, E. & Grunlan, J. Amine salt thickening of intumescent multilayer flame retardant treatment. *Ind. Eng. Chem. Res.* **59**, 2689–2695 (2020).
27. Manion, J. G., Gao, D., Brodersen, P. M. & Seferos, D. S. Insulating polymer additives in small molecule and polymer photovoltaics: how they are tolerated and their use as potential interlayers. *J. Mater. Chem. C* **5**, 3315–3322 (2017).
28. McPherson, A., Nguyen, C., Cudney, R. & Larson, S. B. The role of small molecule additives and chemical modification in protein crystallization. *Cryst. Growth Des.* **11**, 1469–1474 (2011).
29. Rumer, J. W. et al. Dual function additives: A small molecule crosslinker for enhanced efficiency and stability in organic solar cells. *Adv. Energy Mater.* **5**, 1401426 (2015).
30. Hagen, D. A., Saucier, L. & Grunlan, J. C. Controlling effective aspect ratio and packing of clay with pH for improved gas barrier in nanobrick wall thin films. *ACS Appl. Mater. Interfaces* **6**, 22914–22919 (2014).
31. Priolo, M. A., Holder, K. M., Greenlee, S. M. & Grunlan, J. C. Transparency, gas barrier, and moisture resistance of large-aspect-ratio vermiculite nanobrick wall thin films. *ACS Appl. Mater. Interfaces* **4**, 5529–5533 (2012).
32. Song, Y. et al. Edge charge neutralization of clay for improved oxygen gas barrier in multilayer nanobrick wall thin films. *ACS Appl. Mater. Interfaces* **8**, 34784–34790 (2016).
33. Suvorov, S. A., & Skurikhin, V. V. Vermiculite—A promising material for high-temperature heat insulators. *Refract. Ind. Ceram.* **44**, 186–193 (2003).
34. Mariappan, T. Recent developments of intumescent fire protection coatings for structural steel: A review. *J. Fire Sci.* **34**, 120–163 (2016).
35. Velencoso, M. M., Battig, A., Markwart, J. C., Schartel, B. & Wurm, F. R. Molecular firefighting—How modern phosphorus chemistry can help solve the challenge of flame retardancy. *Angew. Chem. Int. Ed.* **57**, 10450–10467 (2018).
36. Dogan, M., Dogan, S. D., Savas, L. A., Ozcelik, G. & Tayfun, U. Flame retardant effect of boron compounds in polymeric materials. *Composites B Eng.* **222**, 109088 (2021).
37. Myers, R. E., Dickens, E. D., Licursi, E. & Evans, R. E. Ammonium pentaborate: An intumescent flame retardant for thermoplastic polyurethanes. *J. Fire Sci.* **3**, 432–449 (1985).
38. Dong, Z. et al. Effect of boron-based additives on char agglomeration and boron doped carbon microspheres structure from lignin pyrolysis. *Fuel* **303**, 121237 (2021).
39. Levchik, S. V., Levchik, G. F., Balabanovich, A. I., Camino, G. & Costa, L. Mechanistic study of combustion performance and thermal decomposition behaviour of nylon 6 with added halogen-free fire retardants. *Polym. Degrad. Stab.* **54**, 217–222 (1996).
40. Huang, C., Qian, X. & Yang, R. Thermal conductivity of polymers and polymer nanocomposites. *Mater. Sci. Eng. R. Rep.* **132**, 1–22 (2018).
41. Sun, F., Fan, X., Zhang, T., Jiang, P. & Yang, J. Numerical analysis of the influence of pore microstructure on thermal conductivity and Young's modulus of thermal barrier coating. *Ceram. Int.* **46**, 24326–24332 (2020).
42. Zhao, Y. et al. Porous architecture and thermal properties of thermal barrier coatings deposited by suspension plasma spray. *Surf. Coat. Technol.* **386**, 125462 (2020).
43. Machrafi, H. & Lebon, G. Size and porosity effects on thermal conductivity of nanoporous material with an extension to nanoporous particles embedded in a host matrix. *Phys. Lett. A* **379**, 968–973 (2015).
44. Smith, D. S. et al. Thermal conductivity of porous materials. *J. Mater. Res.* **28**, 2260–2272 (2013).
45. Yan, Y. et al. Exploring the effect of porous structure on thermal conductivity in templated mesoporous silica films. *J. Phys. Chem. C* **123**, 21721–21730 (2019).
46. Smith, M. W. et al. Structural analysis of char by Raman spectroscopy: Improving band assignments through computational calculations from first principles. *Carbon* **100**, 678–692 (2016).
47. Gouadec, G. & Colomban, P. Raman Spectroscopy of nanomaterials: How spectra relate to disorder, particle size and mechanical properties. *Prog. Cryst. Growth Charact. Mater.* **53**, 1–56 (2007).
48. Pan, D. et al. Li storage properties of disordered graphene nanosheets. *Chem. Mater.* **21**, 3136–3142 (2009).
49. Antidormi, A., Colombo, L. & Roche, S. Thermal transport in amorphous graphene with varying structural quality. *2D Mater.* **8**, 015028 (2020).
50. Mu, X., Wu, X., Zhang, T., Go, D. B. & Luo, T. Thermal transport in graphene oxide—from ballistic extreme to amorphous limit. *Sci. Rep.* **4**, 3909 (2015).
51. Jang, W.-S. & Grunlan, J. C. Robotic dipping system for layer-by-layer assembly of multifunctional thin films. *Rev. Sci. Instrum.* **76**, 103904 (2005).

ACKNOWLEDGEMENTS

The authors acknowledge infrastructure support from the Texas A&M Engineering Experiment Station (TEES) and the Materials Characterization Facility (MCF) at Texas A&M University.

AUTHOR CONTRIBUTIONS

The authors confirm contribution to the paper as follows: study conception and design: C.T.L. and J.C.G.; data collection: C.T.L.; analysis and interpretation of results: C. T.L. and J.C.G.; draft manuscript preparation: C.T.L. and J.C.G. All authors reviewed the results and approved the final version of the manuscript.

COMPETING INTERESTS

The authors declare no competing interests.

ADDITIONAL INFORMATION

Supplementary information The online version contains supplementary material available at https://doi.org/10.1038/s41529-022-00228-2.

Correspondence and requests for materials should be addressed to Jaime C. Grunlan.

Reprints and permission information is available at http://www.nature.com/reprints

Publisher's note Springer Nature remains neutral with regard to jurisdictional claims in published maps and institutional affiliations.